RESEARCH ARTICLE

NANO · MICRO small
www.small-journal.com

Cu-N Synergism Regulation to Enhance Anionic Redox Reversibility and Activity of Li- and Mn-Rich Layered Oxides Cathode

Zhijun Wu, Chenhui Yan, Panyu Gao, Liaona She, Xin Zhang, Yue Lin, Xuebin Yu, Yongfeng Liu, Wenping Sun, Yinzhu Jiang, Yaxiong Yang,* Mingxia Gao,* and Hongge Pan**

Anionic redox chemistry enables extraordinary capacity for Li- and Mn-rich layered oxides (LMROs) cathodes. Unfortunately, irreversible surface oxygen evolution evokes the pernicious phase transition, structural deterioration, and severe electrode-electrolyte interface side reaction with element dissolution, resulting in fast capacity and voltage fading of LMROs during cycling and hindering its commercialization. Herein, a redox couple strategy is proposed by utilizing copper phthalocyanine (CuPc) to address the irreversibility of anionic redox. The Cu-N synergistic effect of CuPc could not only inhibit surface oxygen evolution by reducing the peroxide ion O_2^{2-} back to lattice oxygen O^{2-}, but also enhance the reaction activity and reversibility of anionic redox in bulk to achieve a higher capacity and cycling stability. Moreover, the CuPc strategy suppresses the interface side reaction and induces the forming of a uniform and robust LiF-rich cathode electrolyte, interphase (CEI) to significantly eliminate transition metal dissolution. As a result, the CuPc-enhanced LMRO cathode shows superb cycling performance with a capacity retention of 95.0% after 500 long-term cycles. This study sheds light on the great effect of N-based redox couple to regulate anionic redox behavior and promote the development of high energy density and high stability LMROs cathode.

1. Introduction

Lithium-ion batteries (LIBs) have been worldwide applied in 3C products, electric vehicles (EVs), and grid energy storage in past decades. However, current commercialized LIBs cannot fulfill the demand for high energy density and power density with the rapid development of modern industrial society.[1–4] As the critical component determining the energy density of LIBs, advanced cathode materials urgently need to be developed, especially to solve the "range anxiety" in EVs.[5–7] From this perspective, Lithium and manganese-rich layered oxides (LMRO) with a formula of $xLi_2MnO_3 \cdot (1\text{-}x)LiTMO_2$ (TM = Ni, Co, Mn, etc.) are considered one of the most promising cathode materials for the next generation advanced LIBs owing to their high capacity (>250 mAh g^{-1}) and high energy density (>1000 Wh kg^{-1}), far exceeding the traditional cathode materials like $LiCoO_2$, $LiFePO_4$ and Ni-rich cathode.[8–14] Based on extensive research, it is consensus that the extraordinarily high capacity of LMROs originated from the hybrid cationic and anionic redox reaction, and the anionic redox triggered above 4.4 V involves reversible oxygen redox occurring in the bulk ($O^{2-} \rightarrow O_2^{2-}$) and irreversible oxygen gas release on the surface ($O^{2-} \rightarrow O_2$).[15–18]

Although LMROs have advantages in capacity and cost, several inherent drawbacks still hinder the road to commercialization.

Z. Wu, C. Yan, L. She, Y. Yang, H. Pan
Institute of Science and Technology for New Energy
Xi'an Technological University
Xi'an 710021, China
E-mail: sheliaona@xatu.edu.cn; yangyaxiong@xatu.edu.cn; honggepan@zju.edu.cn

C. Yan, X. Zhang, Y. Liu, W. Sun, Y. Jiang, M. Gao, H. Pan
State Key Laboratory of Silicon and Advanced Semiconductor Materials and School of Materials Science and Engineering
Zhejiang University
Hangzhou 310027, China
E-mail: gaomx@zju.edu.cn

P. Gao, X. Yu
Department of Materials Science
Fudan University
Shanghai 200433, China

Y. Lin
Hefei National Laboratory for Physical Sciences at the Microscale
University of Science and Technology of China
Hefei 230026, China

The ORCID identification number(s) for the author(s) of this article can be found under https://doi.org/10.1002/smll.202401645

DOI: 10.1002/smll.202401645

First, irreversible oxygen release substantially damages the lattice crystal and facilitates transition metal migration to neighboring Li slabs, engendering layered-spinel phase transition, resulting in cathode degradation and capacity/voltage fading.[19–22] Second, oxygen loss would evoke the continual reduction of transition metal to charge compensation, which activates the cation redox reaction of Co^{2+}/Co^{3+} and $Mn^{3+}/^{4+}$, directly leading to the voltage fade.[23] Finally, the interface side reaction deteriorates LMROs as well. The releasing O_2 in the form of oxygen radical and O_2·singlet will attack organic species, such as ethylene carbonate (EC), dimethyl carbonate (DMC), and diethyl carbonate (DEC) and lead to their decomposition and the formation of thick solid cathode-electrolyte interphase (CEI) layer on the surface, resulting in inferior Li^+ diffusions and poor cyclability.[24,25] Moreover, LMROs also suffered from surface structure degradation and transition metal dissolution originating from HF corrosion due to the decomposition of $LiPF_6$.[26,27] Therefore, suppression of oxygen release and side reaction, and construction of uniform and stable CEI layer are vital to enable the practical application of LMROs material.

Various strategies have been employed to solve the drawbacks of LMROs, including surface modification,[28,29] element doping,[30,31] structure design,[32,33] binder readjustment,[34,35] and electrolyte optimization.[25,36] Nonetheless, the mentioned strategies still have shortcomings in the complicated method, ineffective protection, and limited improvement of cyclic stability.

The redox couple strategy has been proven to be a facile and efficacious approach to inhibit oxygen release and achieve outstanding electrochemical stability via chemically reducing the peroxide ion O_2^{2-} back to stable lattice O^{2-} during the discharging process.[37] However, previous research mainly focuses on sulfur elements and lacks discovery of other possible redox couples. Phthalocyanine as one type of porphyrin with an 18 π electron aromatic cloud around the macrocycle has a N-redox activity,[38,39] and is widely applied in organic transistors, organic photovoltaics, and organic light-emitting diodes.[40–43] Inspired by this, herein, we introduce copper phthalocyanine (CuPc, $C_{32}H_{16}CuN_8$) and other metal phthalocyanine derivatives into LMROs and find that CuPc serves as the best redox couple. Detailed structural and chemical characterizations combined with electrochemical testing confirm that the N element in CuPc can serve as a redox activity center to reduce surface O_2^{2-} to O^{2-}, and a synergistic effect of Cu and N element ensures the reaction reversibility of CuPc, thus suppressing surface oxygen evolution and structural degradation. Moreover, CuPc can induce the formation of a uniform and robust LiF-rich CEI on the electrode surface suppress the transition metal dissolution, and prevent the cathode against side reactions. As a result, CuPc-enhanced electrodes exhibit excellent structural stability and deliver outstanding electrochemical performance with higher capacity and voltage retention.

2. Results and Discussion

The X-ray diffraction (XRD) patterns shown in Figure S1 (Supporting Information) show that a new diffraction peak appears when the amount of CuPc added increases (≥5 wt%), but the LMRO and CuPc-enhanced electrodes display the same diffraction reflection. The Rietveld refinements (Figure S2 and Table S1, Supporting Information) further confirm that the lattice parameters of LMRO and LMRO@7CuPc electrodes keep well, indicating preparation process does not damage the bulk structure. **Figure 1**a–c shows the high-angle annular dark field-scanning transmission electron microscopy (HAADF-STEM) images of the as-prepared LMRO@7CuPc electrode. The particle has a coating layer with ≈2 nm, while the bulk presents a layered structure with the interplanar spacing of 2.34 Å corresponding to the (012) plane. STEM-energy dispersive spectroscopy (STEM-EDS) in Figure 1d reveals the elements of Mn, Ni, Co, O, and Cu and N of CuPc are uniformly distributed in the particle, confirming that CuPc is coated on the surface of the LMRO particle.

The electrochemical performances of CuPc-enhanced electrodes in the voltage window of 2.0–4.8 V at 0.1 C and 1 C (1C = 200 mA g^{-1}) are shown in **Figure 2**, and corresponding data are summarized in Table S2 (Supporting Information). Figure 2a shows the initial charge-discharge profile at 0.1 C. All electrodes display typical redox features of Li-rich cathode with a slope region below 4.4 V associated with $Ni^{2+/3+/4+}$ and $Co^{3+/4+}$ cationic redox, and a long plateau ≈4.5 V associated with oxygen redox reaction.[16] Corresponding dQ/dV curves (Figure S3, Supporting Information) well reflect these redox processes and CuPc enhanced electrodes show no new redox reaction peak appears, and the peak area is almost uniform at ≈4.5 V during initial cycle, indicating that redox couple increases the redox reversibility of lattice oxygen during initial cycle, but does not increase the capacity because the introduction of the surface redox couple, the charge-transfer resistance of the electrode is increased since the surface coating layer is insulating. Therefore, the lithiation/delithiation process in $Li_{1.2}Ni_{0.13}Co_{0.13}Mn_{0.54}O_2$ is not changed after the incorporation of CuPc, and the capacities have come from LMRO itself. The initial discharge capacities are 272.8, 273.2, 273.4, 278.5 and 267.7 mAh g^{-1} for LMRO, LMRO@3CuPc, LMRO@5CuPc, LMRO@7CuPc and LMRO@9CuPc electrodes with close initial Coulombic efficiency (ICE) of 75.9%, 75.0%, 75.5%, 78.1% and 72.3%, respectively. That's because the abundant oxygen-related intermediate species are generated during high-voltage oxidation in lithium-rich layer oxide cathodes. These intermediates include lattice oxygen ions (O_n^-), superoxo (O_2^-), peroxo (O_2^{2-}), oxygen vacancies (O-vacancies), O_2 dimers, or lost O_2, which pose a significant challenge to the stability of the electrolyte and cathode-electrolyte interface of LMRO. In particular, nucleophilic species such as peroxo and superoxide can preferentially react with certain solvents, altering the way CEI forms, which results in low Coulombic efficiency.[44–46] The capacity of the LMRO electrode shows a variation of first increasing and then decreasing with the increase of CuPc content and 7 wt% CuPc is considered as the optimum content, which is due to the introduction of the surface redox couple, the charge-transfer resistance of the electrode is increased since the surface coating layer is insulating. In addition, the charge-transfer resistance is gradually decreased, which is accompanied by the increase of discharge capacity during the initial cycling. As shown in Figure 2b, after 50 cycles at 0.1 C, the capacity of the LMRO electrode drops to 233.4 mAh g^{-1} with a retention of 85.6%. Whereas, LMRO@7CuPc shows more steady cycling and remains at a capacity of 264.6 mAh g^{-1} with a retention of 91.8% compared to the maximum capacity of the eighth cycle, indicating excellent cycling stability. The long-term cycling performances are also illustrated in Figure 2c–f. It is ob-

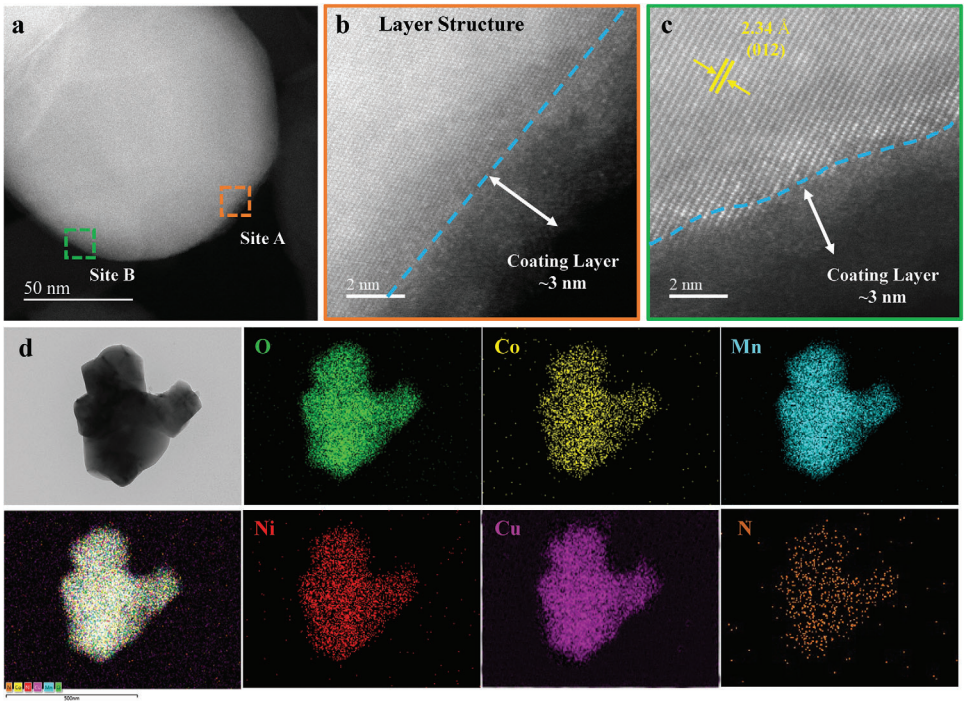

Figure 1. a) HAADF-STEM image of the LMRO@7CuPc electrode. b) Atomic-resolution HAADF-STEM image of the site A in (a). c) Atomic-resolution HAADF-STEM image of the site B in (a). d) STEM-EDS mapping of the LMRO@7CuPc electrode.

vious that LMRO electrode shows extremely fast capacity fading from 214.2 to 119.6 mAh g^{-1}, with a poor retention of only 55.8% after 500 cycles, and the discharge curves (Figure 2d) show severe voltage decay with a voltage retention of 73.9%, indicating that LMRO suffers sever spinel phase transition and structure degradation upon cycling. In sharp contrast, CuPc-enhanced electrodes all exhibit significantly improved cycling stability. In particular, LMRO@7CuPc shows the best cycling performance and delivers steady capacity with only a slight decrease from 224.2 to 213.0 mAh g^{-1} upon 500 cycles with the highest capacity retention of 95.0%. Besides, the voltage decay is also remarkably suppressed maintaining 80.3% (Figure 2e), demonstrating the substantially suppressed of irreversible oxygen evolution and structural degradation during the cycle. Controlling oxygen release and regulating the covalency of the TM—O bond in the material is key to achieving electrochemical stability in LMRO. Cu^{2+} doping is considered to be an effective method for stabilizing the structure of close-packed oxygen and improving the local electronic structure, and it can effectively suppress voltage decay in LMRO.[47–49] Benefiting from improved capacity and voltage cycling stability, CuPc-enhanced electrodes exhibit higher energy density (Figure 2f). After 500 long-term cycles, LMRO@7CuPc still delivers energy density as high as 615.4 Wh kg^{-1}, nearly twice that of LMRO electrode (327.8 Wh kg^{-1}). Compared with the electrochemical performance of the previously reported LMROs (Table S3, Supporting Information), our results clearly exhibit the best cycling performance by far.

Furthermore, other metal phthalocyanine derivatives are investigated using as redox couple in LMRO as well, including phthalocyanine (Pc), nickel phthalocyanine (NiPc), cooper phthalocyanine (CoPc), manganese phthalocyanine (MnPc), iron phthalocyanine (FePc) and zinc phthalocyanine (ZnPc). All the additives are added into LMRO and the electrode preparation are same as CuPc enhanced electrodes, and the corresponding electrochemical performance data are shown in Figures S4 and S5 and Table S4 (Supporting Information). Interestingly, all the metal phthalocyanine derivatives display the enhancement in cycling stability of the LMRO cathode, and the electrochemical performance at the optimum content of each additive is selected for a more intuitive comparison. All electrodes exhibit similar initial charge-discharge profiles, but modified electrodes deliver higher capacities and ICE, especially for MnPc-enhanced electrodes with 283.6 mAh g^{-1} and 81.9%, respectively. The long-term cycling measurement further confirms the positive effect of metal phthalocyanine derivatives on LMRO that each additive-enhanced electrode exhibits higher discharge capacity and improved cycling stability. Among them, CuPc enhanced electrode shows the highest capacity and the best cycling stability (213.0 mAh g^{-1} with 95.0% after 500 cycles). Followed by the FePc and MnPc, corresponding electrodes show also high capacity retention of 87.9% and 86.7%, respectively, with a slightly lower capacity unfortunately. Then the CoPc and Pc enhanced electrodes are in the third echelon, delivering a capacity retention of 84.0% and 80.5%. ZnPc and NiPc enhanced electrodes fall behind others, nevertheless, the capacity stability is still better compared to bare LMRO. In a short summary, the above results clearly confirm the availability and universality of metal phthalocyanine derivatives strategy on LMRO, and the modification effect of most phthalocyanine compounds containing metal ions is better than that of phthalocyanine.

According to the above discussion of electrochemical performance, we speculate that there is a synergetic effect on Cu and

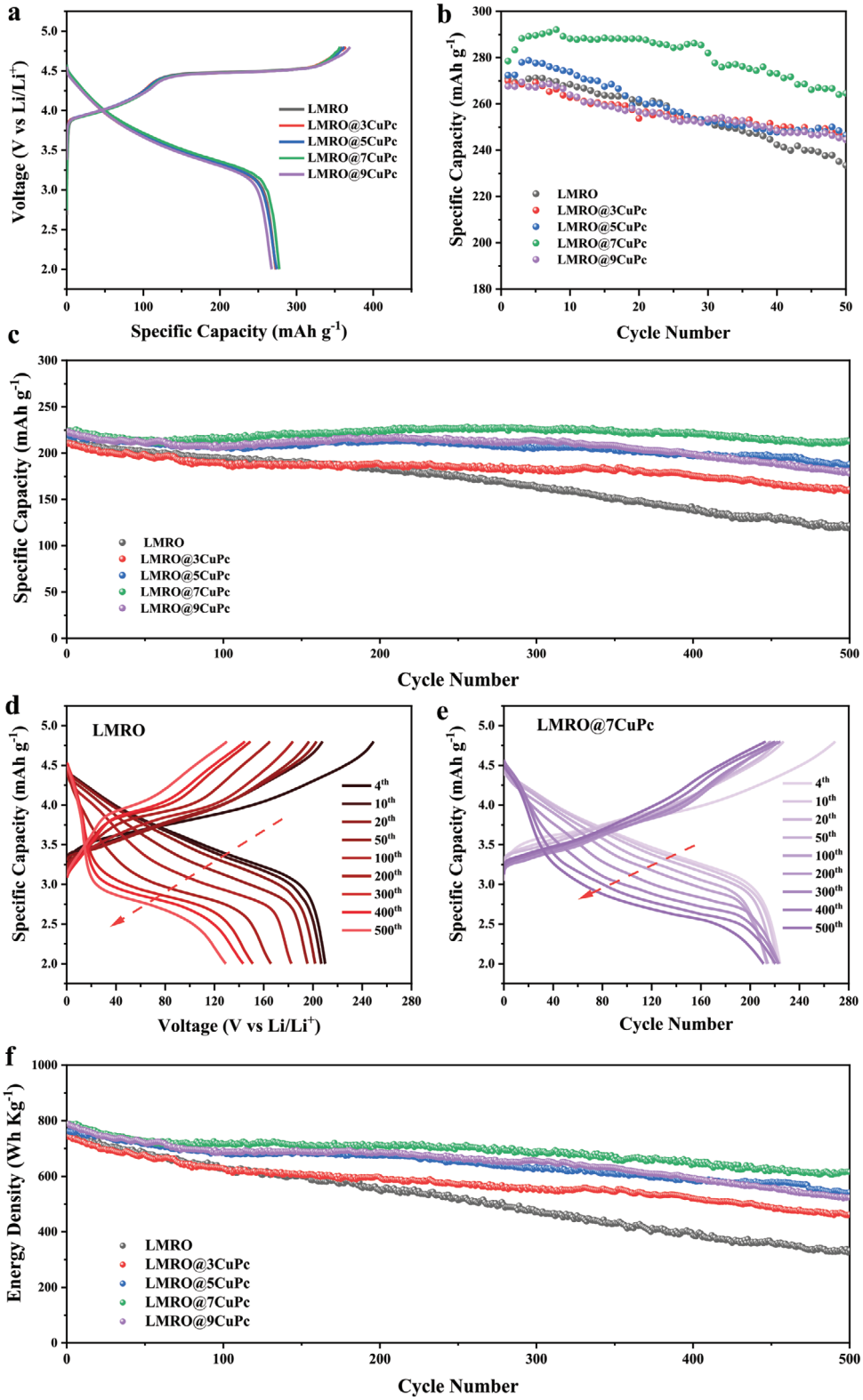

Figure 2. Electrochemical performance of LMRO and CuPc-enhanced electrodes. a) Initial charge–discharge profiles at 20 mA g^{-1}. b) Cycling performance at 20 mA g^{-1}. c) Cycling performance at 200 mA g^{-1}. d,e) Voltage-capacity profiles of LMRO and LMRO@7CuPc electrodes at different cycles. f) Energy density curves during cycling at 200 mA g^{-1}.

N elements of CuPc thus realizing the best cycling stability. To elucidate the mechanism of improved cycling stability and redox behavior of oxygen, X-ray photoelectron spectroscopy (XPS) measurement is conducted for LMRO and LMRO@7CuPc electrodes during the first charge–discharge process. For the O 1s spectra of the surface in Figure S6 (Supporting Information), a new peak located at 530.5 eV related to O_2^{2-} species appears, indicating the oxygen oxidation reaction when charging to 4.8 V[17] and the O_2^{2-} shows less intensity in LMRO@7CuPc electrode, suggesting the difference in surface chemistry. The N 1s spectra are collected in different states of charge (SOC) of LMRO@7CuPc. Before cycling, the electrode exhibits a peak at approximately 399.4 eV (named N_{re}), and when charging above 3.8 V, a new peak at 401.0 eV (N_{ox}) appears to correspond to N losing electrons and oxidation.[43] As an electron donor, the C-N groups (N_{re}) in CuPc easily lose electron oxidation to form C═N (N_{ox}) groups during charging. As an electron acceptor in the discharge process, the electron is reduced back to the C—N groups.[50,51] The intensity of the N_{ox} peak increases accompanied by the decrease of the N_{re} peak during the charging process indicating N element is gradually oxidized, and during the discharging process, the N element is reduced back with the intensity of the N_{ox} peak decreasing again and N_{re} peak becoming dominant. The corresponding atomic ratio of N_{re} and N_{ox} is plotted in **Figure 3c**. It is noted that the ratio during 4.4–4.8 V, corresponding to oxygen redox reaction ($O^{2-} \rightarrow O_2^{2-}$), the ratio of N_{ox} shows a rapid increase. Hence, combined with the above O 1s results, when lattice O^{2-} is oxidized to O_2^{2-} above 4.4 V, the N element can chemically reduce surface O_2^{2-} back to stable lattice O^{2-} again, with generation of oxidized N (N_{ox}), thus inhibiting the irreversible oxygen gas releasing to stabilize crystal structure. The N_{ox} can be reduced back to pristine N_{re} species during the discharging process and play a role in the consequent charge-discharge process complied with the same reaction circulation (Figure S7, Supporting Information). Interestingly, Cu ion displays valence state change and participates in redox reactions as well. As shown in Figure 3b,f, Cu ion exists as Cu^{2+} before the cycle, where the peak at 935.0 eV corresponds to Cu^{2+} $2p_{3/2}$.[52] With the charging, a new peak located at 933.2 eV appears corresponding to Cu^{+} $2p_{3/2}$, indicating the reduction from divalent copper to monovalent copper, which is because the PF_6^- in the electrolyte is easily adsorbated near the copper atoms in CuPc, resulting in a decrease in the charge density of copper, thereby reducing to Cu^+.[39,43] According to previous studies,[53] the N element would combine with PF_6^- when loss electron, and N-PF_6^- interaction may hinder the reduction reaction between N and O_2^{2-}. However, the adsorbed PF_6^- is prone to lie near the Cu atom in CuPc, which allows the N redox activity could be kept by the synergistic effect from the Cu ion to prevent PF_6^- absorption. To further confirm the validity of the Cu/N synergistic effect, the N 1s XPS spectra of phthalocyanine (Pc)-enhanced LMRO electrode are investigated. Compared to CuPc redox couple, Pc has a poor modification on LMRO cathode as discussed above. The N 1s of the LMRO + 1%Pc electrode shows a similar peak variation that N is oxidized during charge and is reduced back during discharge, indicating the redox reaction with O_2^{2-} similar with CuPc (Figure S8, Supporting Information). In sharp contrast, the ratio of N_{ox} is less with a slight change, suggesting the lower reaction activity and reversibility of N in the LMRO + 1%Pc electrode. Therefore, the synergistic effect of Cu and N ensures the high reaction activity of N element to reduce O_2^{2-} of LMRO in time, and the effect of Cu is also maintained in the next cycling (Figure S7, Supporting Information), thus realizing the high performance of CuPc redox couple.

Operando differential electrochemical mass spectrometry (DEMS) was performed to evaluate the gas evolution during the initial cycle. As depicted in Figure 3e, the LMRO electrode displays an obvious O_2 and CO_2 generation when charging above 4.4 V, which originates from the oxidation of surface O_2^{2-} and electrolyte decomposition, respectively. When charging to 4.8 V, O_2 and CO_2 have the largest gas flux with 0.656×10^{-2}, 0.812×10^{-2} μmol min^{-1}, respectively. In contrast, LMRO@7CuPc exhibits significant suppression of gas evolution with the postponement of O_2 and CO_2 generated voltage and the amount of gas is remarkably lower than that of LMRO (only 0.078×10^{-2} and 0.208×10^{-2} μmol min^{-1}), confirming the elimination of oxygen release enabled by CuPc redox couple.

Except for the effect on the LMRO surface, the CuPc strategy enhances the oxygen redox in bulk as well. LMRO and LMRO@7CuPc electrodes in different SOC were etched by Ar ion for 20 min to collect the bulk information of O 1s.[54,55] As shown in Figure 3f,g, during the initial cycle, the O_2^{2-} species (peak at 530.5 eV) gradually generate, increase, and then decrease due to the oxygen redox ($O^{2-} \rightarrow O_2^{2-} \rightarrow O^{2-}$), and the intensity of O_2^{2-} is higher in LMRO@7CuPc, indicating more oxygen redox. To evaluate oxygen redox activity quantitatively, O_2^{2-}%, defined as $(O^{2-}/(O_2^{2-}+O^{2-}))$ by considering the integrated areas, is plotted in Figure S9 (Supporting Information). LMRO shows lower O_2^{2-}% during cycling with a maximum value of 12.41% in 4.8 V, and even 4.45% O_2^{2-} is residual reflecting the partial irreversible reaction. Whereas, LMRO@7CuPc exhibits higher O_2^{2-} ratio with a maximum of 30.84% and full O_2^{2-} is reduced back when discharging to 2.0 V, and the investigation on the second cycle also shows the same pattern (Figure S10, Supporting Information). The above results verify the enhancement of oxygen reaction activity and reversibility benefitted from the CuPc strategy in LMRO bulk. Therefore, the effect of CuPc redox couple could be briefly summarized as that the irreversible oxygen evolution is the elimination of Cu/N synergetic effect on the surface and the oxygen redox activity and reversibility is greatly improved in the inner bulk region, thus achieving outstanding capacity and cycling stability.

To investigate the structural degradation during cycling, XRD patterns of LMRO and LMRO@7CuPc at selected cycles are compared and shown in Figure S11 and Table S1 (Supporting Information). During the cycling, the diffraction reflections of the LMRO electrode gradually weaken and widen, indicating the destruction and disordering of the crystal structure. Besides, according to Rietveld refinement results, the LMRO electrode suffers severe phase transition and a large amount of spinel phase is formed which reaches 34.71 wt% after 500 cycles. Oppositely, the LMRO@7CuPc electrode remains a strong reflection during the cycling process and shows good structure maintenance. Meanwhile, the content of the spinel phase in LMRO@7CuPc shows quite a slow increase, and only 8.24 wt% spinel phase is formed after 500 cycles, indicating the significant suppression of layered spinel phase transition. Moreover, the variation of lattice parameter after 500 cycles confirms LMRO@7CuPc shows a much milder unit cell expansion ratio, only half of that of LMRO.

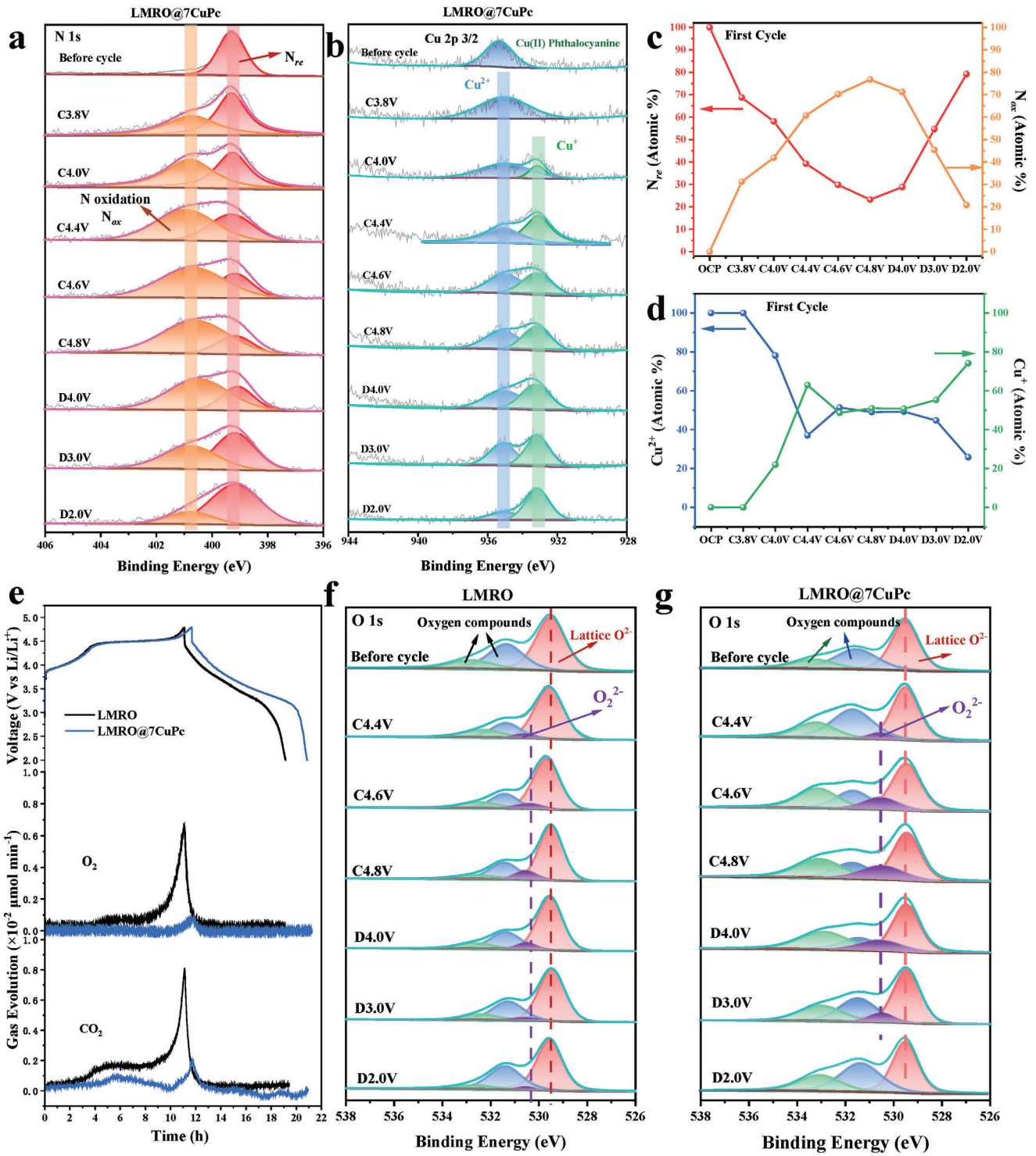

Figure 3. The XPS spectra for LMRO@7CuPc electrode during the first cycle of a) N 1s spectra, b) Cu 2p Spectra. c) Relative atomic ratio of N_{re} and N_{ox} during the first cycle of LMRO@7CuPc electrode. d) Relative atomic ratio of Cu^{2+} and Cu^{+} during the first cycle of LMRO@7CuPc electrode. e) DEMS curves for LMRO and LMRO@7CuPc electrode during the first cycle. The O 1s after Ar etching 20 min during the first cycle for f) LMRO electrode and g) LMRO@7CuPc electrode.

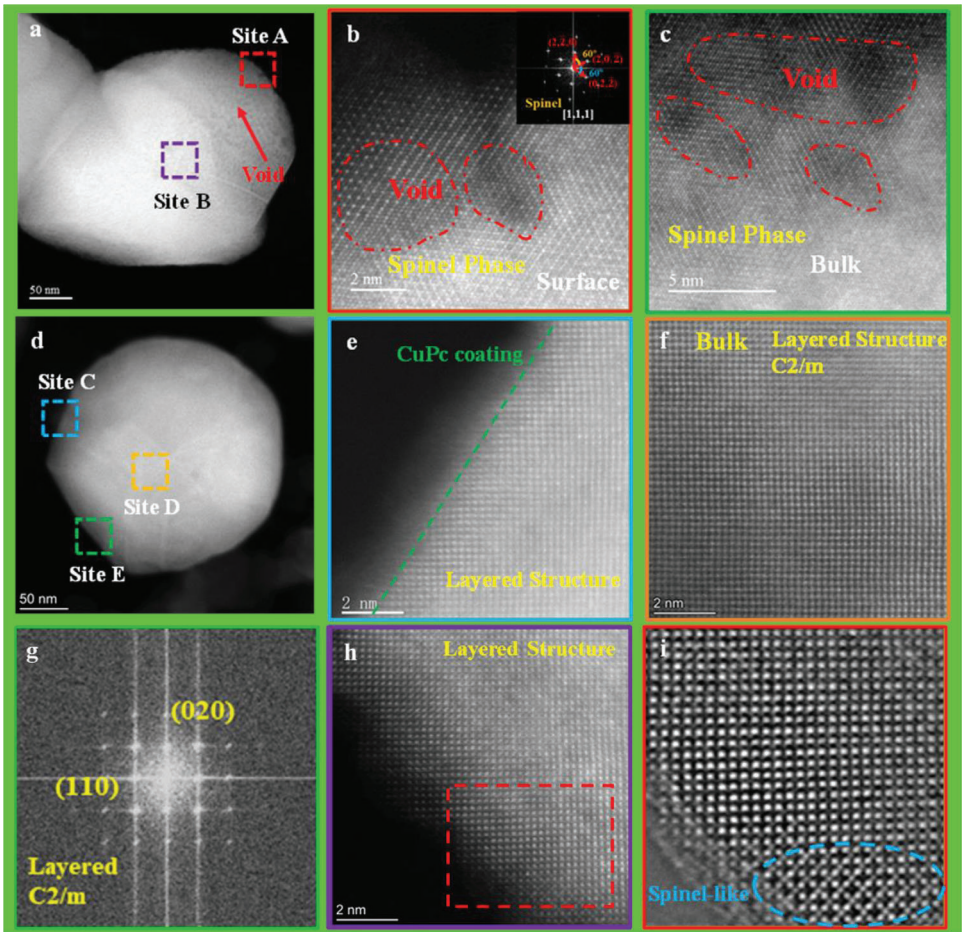

Figure 4. a) HAADF-STEM image of LMRO electrode after 500 cycles. b) Atomic-resolution HAADF-STEM image of site A in (a). Inset: FFT image of Figure b. c) Atomic-resolution HAADF-STEM image of site B in (a). d). HAADF-STEM image of LMRO@7CuPc electrode after 500 cycles. e) Atomic-resolution HAADF-STEM image of site C in (d). f) Atomic-resolution HAADF-STEM image of site D in (d). g) FFT pattern of the purple rectangle region in (f). h) Atomic-resolution HAADF-STEM image of site E in (d). i) iDPC-STEM image of the red rectangle region in (h).

The better structure stability is also proven by surface-sensitive Raman spectrometry as shown in Figure S12 (Supporting Information). For the pristine LMRO electrode, the peak located at 415 cm^{-1} is ascribed to A_{1g} vibration of monoclinic Li_2MnO_3 (C2/m structure), and two peaks located at 475 and 592 cm^{-1} could be attributed to E_g and A_{1g} vibrations of R-3m structure, respectively.[32,56] After 500 cycles, the A1g peak of C2/m vanishes due to the damage to the superstructure, and the peaks of R-3m broaden and appear to redshift with a new strong peak of 625 cm^{-1} related to cubic Fd-3m structure,[56,57] suggesting the degradation of layered structure and sever spinel phase transition, consistent to XRD results, which is because of the oxygen evolution in the charging process, which makes the transition metal become unstable and migrate, causing the transition to the spinel phase.[58,59] In contrast, LMRO@7CuPc exhibits well-preserved E_g and A_{1g} vibration peaks of R-3m as well as A_{1g} vibration of C/2m with tiny cubic Fd-3m peaks, indicating the significant suppression of structure degradation and oxygen evolution.

Furthermore, Atomic-resolution HAADF-STEM is conducted to investigate the structure evolution on the nanoscale. As shown in **Figure** 4a, the LMRO electrode shows a huge morphology change in that the whole particle becomes loose and the surface region becomes rough with jagged edges due to a side reaction with electrolyte.[20] It is worse that lots of nanovoids distribute throughout the particle whether on the surface or in bulk (Figure 4b,c), resulting from irreversible oxygen release and transition metal dissolution. Moreover, fast Fourier transform (FFT) confirms that considerable layered structure has been transformed to the Fd-3m spinel structure with [111] zone axis and spinel phase transition extends from the surface into the bulk in LMRO particle, which is responsible for the fast capacity and voltage fading. In sharp contrast, the cycled LMRO@7CuPc electrode exhibits excellent structural integrity that the particle still maintains a tight structure and no nanovoids form due to the effective suppression of oxygen release (Figure 4d). The oxidized O_2^{2-} would become much more mobile and easier to escape from the surface of particles, resulting in oxygen loss and oxygen vacancies. Once the oxygen vacancies are generated during cycling at the surface of LMROs, the bulk O_2^{2-} will outward diffuse and inject oxygen vacancies into the interior of the particle, consequently leading to continuous oxygen release and oxygen void formation.[60,61] Therefore, suppressing the surface oxygen

release or eliminating the surface O_2^{2-} will shut down the global oxygen migration and contribute to excellent cycling performance. According to the root origin of oxygen release, CuPc redox couple has been proven to be a facile and efficacious approach to inhibit oxygen release.

Further observation on the surface site C reveals that the CuPc coating layer remains yet and the surface region keeps a well-layered structure (Figure 4e). In the inner bulk (site D, Figure f), LMRO@7CuPc retains an intact and ordered structure index to the C2/m space group. Based on the fast Fourier transform (FFT) analysis, the d spacings of 4.21 and 4.08 Å of the core lattice can be attributed to the (020) and (110) planes of the monoclinic C2/m phase (Figure 1g).[62–64] Surface spinel is only observed in a very small region as highlighted in the red dashed box in Figure 4h. The iDPC-STEM image of Figure 4i clearly shows that Li sites are partially occupied by TM ions to form a spinel-like structure, nonetheless. These results demonstrate that the CuPc strategy can significantly inhibit structural degradation and spinel phase transition, realizing superior structural stability. Similarly, Figure S13 (Supporting Information) shows the morphology of LMRO@7CuPc particle surfaces before cycles and after 500 cycles. It is obvious that LMRO@7CuPc maintains smooth particle surfaces as original, which is consistent with HAADF-STEM results.

Electron energy loss spectrometry (EELS) is conducted to evaluate the stability of oxygen lattice and valence states evolution of transition metal, and the line scanning spectra from surface to bulk is depicted in **Figure 5a–f**. The pre-edge of O K-edge spectra in LMRO (Figure 5a), which is associated with the transition of electrons from the O 1s to unoccupied 2p states hybridized within transition metals 3d states,[65] show a gradual suppression of the from the 50-nm-deep bulk to the surface, and vanish on the outmost surface, indicates the deterioration of oxygen lattice due to oxygen gas evolution. The Mn L and Co L-edge spectra (Figure 5a,b) show a shift to lower energy on the surface even extending to 40–50 nm depth bulk, indicating the severe reduction of transition metal valence, blamed for the fast voltage decay. The ratio of Mn L_3 and L_2 reflects the Mn valence states according to the report by Schmid,[66] and it clearly shows Mn is reduced to Mn^{3+} in a nearly 40 nm region (Figure 5c). On the contrary, the oxygen pre-edge of LMRO@7CuPc is maintained well except for a slight decrease on the 6-nm-deep surface region, and the shift to lower energy of Mn L and Co L-edge are limited on 6 nm depth as well (Figure 5d,e). The Mn^{3+} only exists on the 6-nm surface region and Mn^{4+} is preserved well in the inner bulk, indicating the substantial enhancement of oxygen lattice and suppression of transition metal reduction (Figure 5f). EELS mapping analysis in Figure 5g,h provides a visual distribution of Mn valence states on the particle and further confirms that Mn^{3+} pervades the whole particle in LMRO with a thickness of 40 nm, while the Mn^{3+} reduction layer is remarkably limited to 6 nm in LMRO@7CuPc. Benefiting from the preservation of oxygen lattice framework and transition metal valence owning to CuPc redox strategy, LMRO@7CuPc exhibits superior structural stability and mitigated voltage decay.

Another important effect of CuPc modification is that LMRO@7CuPc forms a more stable, uniform, and robust cathode-electrolyte interface shielding the cathode against electrolyte side reactions and suppressing the transition metal dissolution. XPS is conducted to investigate surface compositions of the formed CEI layer for electrodes after 500 cycles as shown in **Figure 6a**. The C 1s spectra of both electrodes have four peaks ascribed to C—C, C—O, C═O, and C—F species,[67] and C—O peaks show less intensity in the LMRO@7CuPc electrode. For O 1s spectra, the peaks located at 529.5, 531.5, 532.3, and 533.5 eV are ascribed to lattice oxygen (TM—O bond), oxygen vacancies, carbonate species (CO_3^{2-}) and electrolyte oxidation species, respectively.[29,68] In both electrodes, the lattice oxygen peak nearly disappears indicating CEI grows and thickens during cycling, the oxidation of lattice oxygen into products such as CO_3^{2-} and electrolyte oxidation species due to corrosion of electrolyte, and finally the formation of oxygen vacancies. It is noted that the atomic ratio of CO_3^{2-} and electrolyte oxidation species in the LMRO@7CuPc electrode are 32.75% and 16.89%, respectively, which is much less than that of the LMRO electrode (44.37% and 30.16%), indicating the alleviation of side reaction. With respect to the P 2p spectra, the peaks around 133.8 and 134.7 eV are ascribed to $Li_xPO_yF_z$, and the peak at 136.3 eV is related to Li_xPF_y.[67] LMRO@7CuPc electrode shows a great distinction compared to LRMO which contains fewer $Li_xPO_yF_z$ species with the absence of the peak at 134.7 eV, indicating the alleviated decomposition of $LiPF_6$ in the electrolyte. Besides, F 1s spectra manifest that LiF-rich CEI forms on the surface of the LMRO@7CuPc electrode. LiF-rich CEI suffers less strain during cycling thus keeping a stable structure to prevent the cathode particle from electrolyte side reaction and HF corrosion.[69] Furthermore, time-of-flight secondary ion mass spectrometry (TOF-SIMS) data are collected to investigate CEI structures and secondary ion maps are illustrated in Figure 6b and Figure S15 (Supporting Information). LMRO@7CuPc electrode shows a much even distribution of LiF_2^-, which is predominantly from LiF, suggesting uniform LiF-rich CEI consistent with the results of XPS. The contents of organic species including C_2HO^-, $C_2H_3O^-$, CHO_2^-, CHO_2^- and $C_2H_3O_2^-$ show less accumulation in the LMRO@7CuPc compared to the LMRO electrode, indicating the suppressed decomposition of ethylene carbonate (EC) and diethyl carbonate (DEC) benefitted from inhabitation of oxygen release which will attack electrolyte.[70] Besides, P-containing species in CEI have also been significantly changed. The PO_3^-, PF_6^-, PO_2^-, PO^- and $PF_2O_2^-$ originated from the decomposition of $LiPF_6$ are much less intense in LMRO@7CuPc than those in LMRO. Moreover, the F-containing species including F- and TMF_3^- (NiF_3^-, CoF_3^- and MnF_3^-) show a greatly reduce for the LMRO@7CuPc electrode. HF, generated from the decomposition of $LiPF_6$, would corrode LMRO materials during the electrochemical process, causing electrode structure degradation.[26,71,72] The reduced contents of TMF_3^- in LMRO@7CuPc substantially prove that transition metal corrosion and dissolution are significantly suppressed.[73] To further evaluate the element dissolution in detail, EDS line scanning from surface to bulk is performed as shown in Figure 6c,d). The LMRO electrode shows an obvious element depletion layer of O, Ni, Co, and Mn with a thickness of ≈73 nm, resulting from irreversible oxygen release and transition metal dissolution. In contrast, the element depletion layer is much thinner in LMRO@7CuPc with only 26 nm, suggesting the better preservation of the element. Inductively coupled plasma optical emission spectrometry (ICP-OES) is conducted to assess the transition

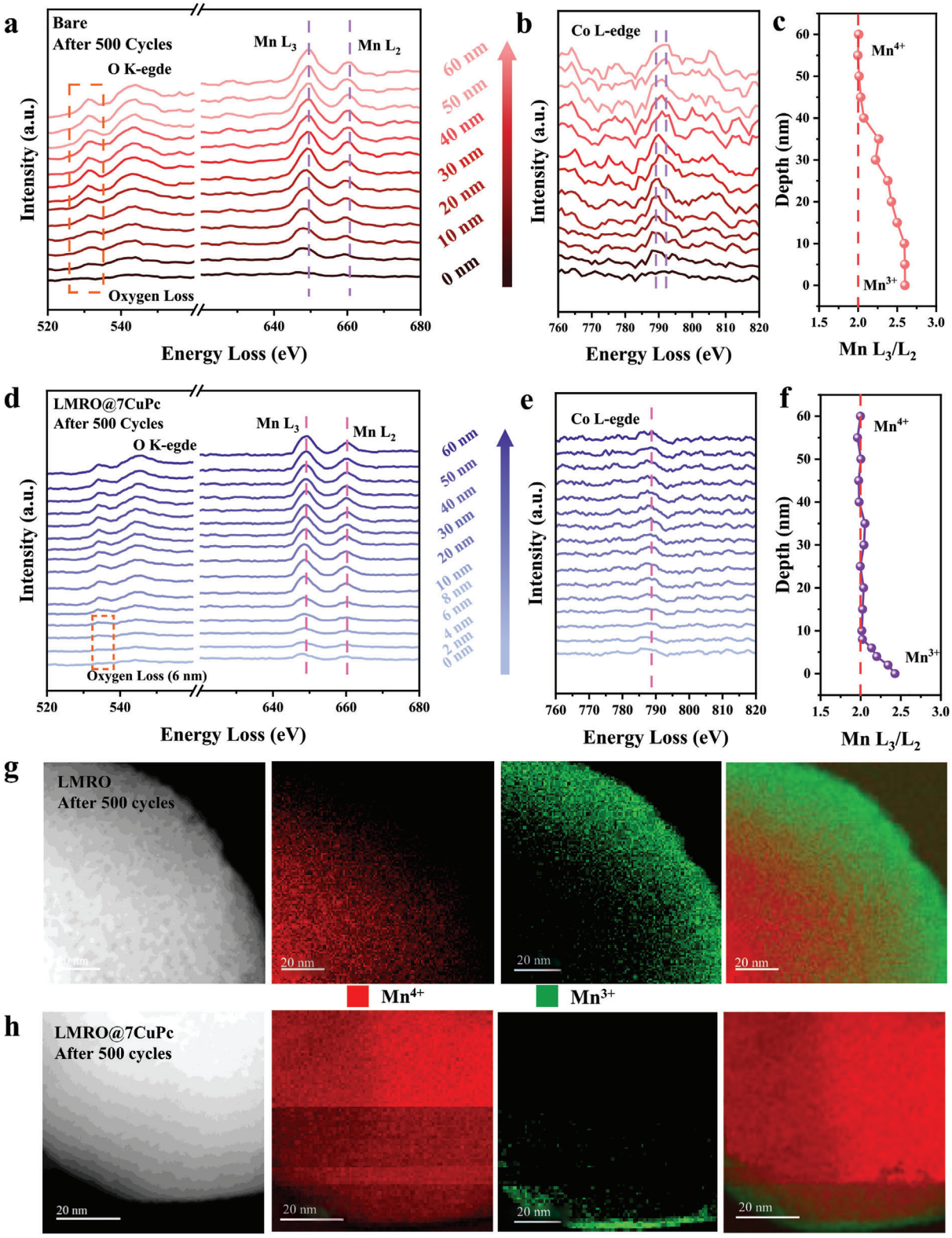

Figure 5. a–c) EELS line scanning from the surface into the bulk of the LMRO electrode after 500 cycles. d–f) EELS line scanning from the surface into the bulk of LMRO@7CuPc electrode after 500 cycles. The corresponding EELS scanning pathway is shown in Figure S14 (Supporting Information). g) EELS mapping for Mn^{4+} and Mn^{3+} of LMRO electrode after 500 cycles. h) EELS mapping for Mn^{4+} and Mn^{3+} of LMRO@7CuPc electrode after 500 cycles.

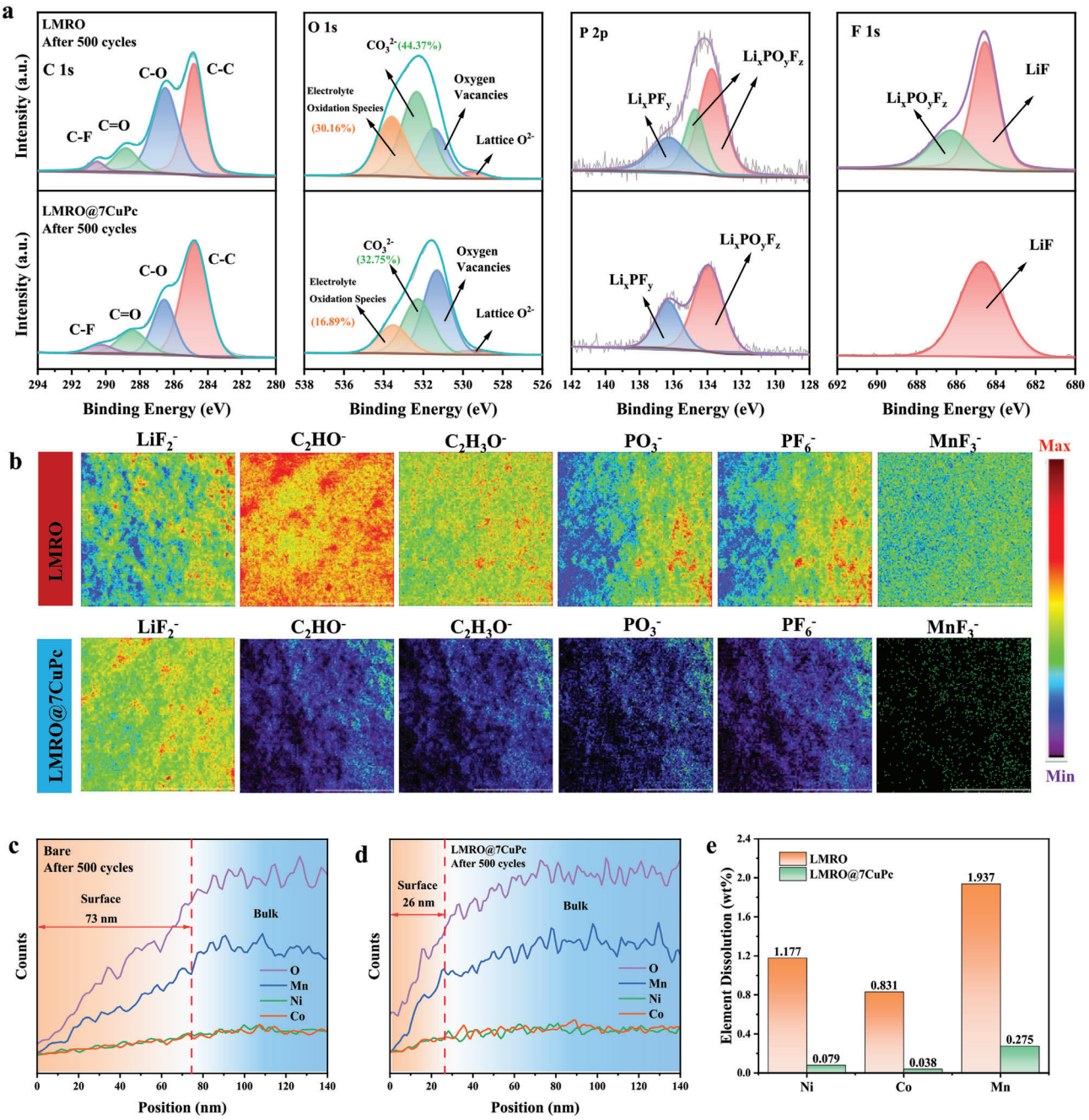

Figure 6. a) C 1s, O 1s, P 2p, and F 1s high-resolution XPS spectra of LMRO (top) and LMRO@7CuPc (bottom) after 500 cycles. b) TOF-SIMS investigations CEI structure after 500 cycles. The mapping for LiF^-, C_2HO^-, $C_2H_3O^-$, PO_3^-, PF_6^- and MnF_3^- secondary ions for LMRO electrode (top) and LMRO@7CuPc electrode (bottom). The secondary ion maps were acquired in a 200 μm × 200 μm region. STEM-EDS line scanning for c) LMRO electrode and d) LMRO@7CuPc electrode after 500 cycles. e) The dissolubilities of TM elements from the LMRO and LMRO@7CuPc electrodes after 500 cycles.

metal dissolution quantificationally. The dissolution ratios of Ni, Co, and Mn for LMRO electrode are as high as 1.177, 0.831, and 1.937 wt%, respectively, while the corresponding dissolution ratios of TM elements for LMRO@7CuPcelectrode are only 0.079, 0.038, and 0.275 wt%, respectively. It is worth noting that the inhibition effect on the dissolution of Ni and Co elements is more significant, which is conducive to the retention of cationic redox reaction thus maintaining electrode capacity. The above results demonstrate that the CuPc strategy can effectively restrain the decomposition of electrolytes and induce the formation of a more uniform and robust LiF-rich CEI, thus improving the surface chemistry stability and suppressing transition metal dissolution, hence realizing steady electrochemical performance.

3. Conclusion

In summary, we first develop CuPc as a redox couple to LMRO cathode by a facile and effective method and realize outstanding electrochemical performance with improved capacity and voltage stability. The LMRO@7CuPc maintains over 95.0% capacity retention and 80.3% voltage retention after 500 cycles at 200 mA g^{-1}. The underlying mechanism of the CuPc redox couple strategy is comprehensively researched with various advanced characterizations and could be summarized as follows. On the one hand, the N ion in CuPc can reduce the O_2^{2-} back to lattice O^{2-} in time during the charging process to prevent oxygen release, and the oxidized N ion can be reduced back during the discharge process and hence participate in the subsequent redox cycle, meanwhile, Cu ion also plays an important role in the above process to improve the reaction reversibility of N ion. The synergistic effect of Cu and N achieves significant suppression of oxygen evolution, thus alleviating structure degradation, spinel phase transition, and transition metal valence reduction. On the other hand, the CuPc strategy inhibits electrolyte decomposition and induces the formation of a uniform and robust LiF-rich CEI, which suppresses side reactions and transition metal dissolution effectively. Furthermore, the comparison between CuPc and other metal phthalocyanine derivatives reveals that dual element redox couple possessing synergistic effect is more desirable for enhancing LMRO performance, and it's believed that these findings may shed light on subsequent redox couple research.

4. Experimental Section

Synthesis of Samples: The $Li_{1.2}Ni_{0.13}Co_{0.13}Mn_{0.54}O_2$ material was synthesized by spray pyrolysis followed by high-temperature calcination. Lithium acetate dihydrate (LiAC·$2H_2O$, AR), manganese acetate tetrahydrate ($Mn(AC)_2·4H_2O$, AR), cobalt acetate tetrahydrate ($Co(AC)_2·4H_2O$, AR) and nickel acetate tetrahydrate ($Ni(AC)_2·4H_2O$, AR) used as the starting materials with a molar ratio of Li: Ni: Co: Mn = 1.2:0.13:0.13:0.54 were added into 2 L deionized water in a concentration of 0.3 mol L^{-1}, and 0.8 mol citric acid was added into solution to inhibit the precipitation of metal salts. The mixed solution was stirred for 1 h, and then the spray solution was sent to the pulverizer with a high-press gas of 200 °C by a peristaltic pump to obtain precursor powders. The collected precursor powders were then calcined at 900 °C for 10 h in air to obtain LMRO material.

Preparation of Electrodes: LMRO (1.6 g) and conductive additive Super P (TIMCAL) (0.2 g) were mixed via the ball-milling method in a stainless-steel ball mill jar (120 mL) adding tungsten carbide balls (108 g) and ethanol (80 mL) with 400 r min^{-1} for 6 h. The obtained mixed materials were dried at 80 °C in an air-circulation oven for 12 h. Then the obtained mixed materials and binder sodium carboxymethyl cellulose (CMC), CuPc (Macklin, β-form, 90%) with a weight ratio of (95-x):5:x (x = 0,3, 5, 7, 9) were mixed with magnetic stirring for 6 h and cast onto an aluminum foil and then dried at 120 °C in a vacuum oven for 20 h. CMC is a better binder for LMRO, which can not only stabilize the electrode structure by preventing the electrode materials from detaching from the current collector but also suppress the voltage fading of the LMRO cathode due to Na^+ ions doping. Most importantly, the dissolution of metal elements from the cathode materials into the electrolyte is also inhibited.[74] The mass loading of the electrode is 2.20 mg cm^{-2}. The other enhanced electrodes are prepared in the same way by adding Pc, MnPc, FePc, CoPc, NiPc, and ZnPc, respectively.

Material Structure Characterizations: XRD analysis was performed on a Mini Flex 600 X-ray diffractometer (Rigaku, Japan) with Cu-K_α radiation operating at a voltage of 40 kV and current of 15 mA with 2θ ranging from 10° to 60° at a scan rate of 1° min^{-1}. Rietveld refinements of the XRD data were carried out by a General Structure Analysis System (GSAS) software package. HAADF-STEM images, STEM-EDS, and EELS spectra were obtained in the JEM-ARM200F microscope, Spectra 300 microscope, and FEI Talos F200x. The Operando differential electrochemical mass spectrometry (DEMS) was performed in an i-DEMS 100 instrument (Linglu Instruments Co. Lt, Shanghai) with an EI-70 eV ion source and SEM-1100v detector. The cells were assembled in Swagelok-type cells and tested under an Ar gas flow of 0.9 mL mi^{-1}n at a current density of 40 mA g^{-1} at the voltage range of 2.0–4.8 V using LAND CT2001A. XPS measurements were performed using an X-ray photoelectron spectrometer (Thermo Scientific K-Alpha) equipped with an Al Kα X-ray radiation source (photon energy 1486.6 eV). The collected data were calibrated against the C 1s peak at 284.8 eV. Raman spectrometry was measured in measured on a Renishaw inVia with a 532 nm excitation wavelength. TOF-SIMS analysis was performed on PHI nanoTOF II Time-of-Flight SIMS with pulsed 30 keV Bi_3^{++} ion beam in a high mass resolution mode. All detected secondary ions of interest have a mass range of 2–1850 aum and possess negative polarity over an area of 200 µm × 200 µm. To measure the amount of deposited transition metal, the lithium foil of the cycled cell was dissolved in 10 mL HNO_3 and analyzed by ICP-OES (Thermo Fisher iCAP PRO).

Electrochemical Measurements: The electrochemical performance was characterized by 2025 coin-type cells. These cells were assembled in an Ar-filled glove box (water and oxygen content < 0.1 ppm) with lithium metal foil as the counter electrode, and Celgard-2400 membrane as a separator. A solution of 1 M $LiPF_6$ in ethylene carbonate (EC), ethyl methyl carbonate (EMC), and diethyl carbonate (DEC) with a volume ratio of 1:1:1 was used as electrolyte. Galvanostatic charge and discharge tests were performed on a multi-channel battery testing system (NEWARE BST-610, China) at different currents with a potential window of 2.0–4.8 V versus Li/Li^+ at 30 °C. The standard sample (LMRO) data used in this paper is consistent with the previous work in order to compare the consistency of data.[75]

Supporting Information

Supporting Information is available from the Wiley Online Library or from the author.

Acknowledgements

Z.J.W. and C.H.Y. contributed equally to this work. The authors gratefully acknowledge the financial support from the National Key Research and Development Program of China (2022YFB2502000), the National Natural Science Foundation of China (52201277), the key program of the National Natural Science Foundation of China (51831009), the National Outstanding Youth Foundation of China (52125104).

Conflict of Interest

The authors declare no conflict of interest.

Data Availability Statement

The data that support the findings of this study are available from the corresponding author upon reasonable request.

Keywords

copper phthalocyanine, Cu-N synergism, cycling stability, Li- and Mn-rich layered oxide, redox couple

Received: March 2, 2024
Revised: April 27, 2024
Published online: May 19, 2024

[1] J. Xu, J. Zhang, T. P. Pollard, Q. Li, S. Tan, S. Hou, H. Wan, F. Chen, H. He, E. Hu, *Nature* **2023**, *614*, 694.
[2] J. Xu, X. Cai, S. Cai, Y. Shao, C. Hu, S. Lu, S. Ding, *Energy & Environmental Materials* **2023**, *6*, e12450.
[3] Z. Cui, A. Manthiram, *Angew. Chem., Int. Ed.* **2023**, *62*, e202307243.
[4] G. Ji, J. Wang, Z. Liang, K. Jia, J. Ma, Z. Zhuang, G. Zhou, H.-M. Cheng, *Nat. Commun.* **2023**, *14*, 584.
[5] R. Schmuch, R. Wagner, G. Horpel, T. Placke, M. Winter, *Nat. Energy* **2018**, *3*, 267.
[6] Y. X. Yao, X. Chen, N. Yao, J. H. Gao, G. Xu, J. F. Ding, C. L. Song, W. L. Cai, C. Yan, Q. Zhang, *Angew. Chem., Int. Ed.* **2023**, *62*, e202214828.
[7] Y. Che, X. Hu, X. Lin, J. Guo, R. Teodorescu, *Energy Environ. Sci.* **2023**, *16*, 338.
[8] J. Sun, X. Z. Xiao, Z. J. Zheng, X. L. Fan, C. C. Xu, L. X. Liu, S. Q. Li, L. X. Chen, *Rare Metals.* **2017**, *36*, 77.
[9] W. He, W. Guo, H. Wu, L. Lin, Q. Liu, X. Han, Q. Xie, P. Liu, H. Zheng, L. Wang, X. Yu, D.-L. Peng, *Adv. Mater.* **2021**, *33*, 2005937.
[10] W. H. Zuo, M. Z. Luo, X. S. Liu, J. Wu, H. D. Liu, J. Li, M. Winter, R. Q. Fu, W. L. Yang, Y. Yang, *Energy Environ. Sci.* **2020**, *13*, 4450.
[11] W. B. Du, Q. N. Shao, Y. Q. Wei, C. H. Yan, P. Y. Gao, Y. Lin, Y. Z. Jiang, Y. F. Liu, X. B. Yu, M. X. Gao, W. P. Sun, H. G. Pan, *ACS Energy Lett.* **2022**, *7*, 3006.
[12] S. Kang, D. Choi, H. Lee, B. Choi, Y. M. Kang, *Adv. Mater.* **2023**, *35*, 2211965.
[13] J. Song, F. Ning, Y. Zuo, A. Li, H. Wang, K. Zhang, T. Yang, Y. Yang, C. Gao, W. Xiao, *Adv. Mater.* **2023**, *35*, 2208726.
[14] B. Li, G. Rousse, L. Zhang, M. Avdeev, M. Deschamps, A. M. Abakumov, J.-M. Tarascon, *Energy Environ. Sci.* **2023**, *16*, 1210.
[15] C. X. Zhang, B. Wei, M. Y. Wang, D. T. Zhang, T. Uchiyama, C. P. Liang, L. B. Chen, Y. Uchimoto, R. F. Zhang, P. Wang, W. F. Wei, *Energy Storage Mater.* **2022**, *46*, 512.
[16] K. Luo, M. R. Roberts, R. Hao, N. Guerrini, D. M. Pickup, Y.-S. Liu, K. Edström, J. Guo, A. V. Chadwick, L. C. Duda, P. G. Bruce, *Nat. Chem.* **2016**, *8*, 684.
[17] G. Assat, D. Foix, C. Delacourt, A. Iadecola, R. Dedryvère, J.-M. Tarascon, *Nat. Commun.* **2017**, *8*, 2219.
[18] G. Assat, J. M. Tarascon, *Nat. Energy* **2018**, *3*, 373.
[19] P. M. Csernica, S. S. Kalirai, W. E. Gent, K. Lim, Y. S. Yu, Y. Z. Liu, S. J. Ahn, E. Kaeli, X. Xu, K. H. Stone, A. F. Marshall, R. Sinclair, D. A. Shapiro, M. F. Toney, W. C. Chueh, *Nature Energy.* **2021**, *6*, 642.
[20] P. F. Yan, J. M. Zheng, Z. K. Tang, A. Devaraj, G. Y. Chen, K. Amine, J. G. Zhang, L. M. Liu, C. M. Wang, *Nat. Nanotechnol.* **2019**, *14*, 602.
[21] M. Gu, I. Belharouak, J. M. Zheng, H. M. Wu, J. Xiao, A. Genc, K. Amine, S. Thevuthasan, D. R. Baer, J. G. Zhang, N. D. Browning, J. Liu, C. M. Wang, *ACS Nano* **2013**, *7*, 760.
[22] S. Sharifi-Asl, V. Yurkiv, A. Gutierrez, M. Cheng, M. Balasubramanian, F. Mashayek, J. Croy, R. Shahbazian-Yassar, *Nano Lett.* **2020**, *20*, 1208.
[23] E. Y. Hu, X. Q. Yu, R. Q. Lin, X. X. Bi, J. Lu, S. M. Bak, K. W. Nam, H. L. L. Xin, C. Jaye, D. A. Fischer, K. Amine, X. Q. Yang, *Nat. Energy* **2018**, *3*, 690.
[24] Z. W. Zhang, J. L. Yang, W. Huang, H. S. Wang, W. J. Zhou, Y. B. Li, Y. Z. Li, J. W. Xu, W. X. Huang, W. Chiu, Y. Cui, *Matter.* **2021**, *4*, 302.
[25] Y. X. Li, W. K. Li, R. Shimizu, D. Y. Cheng, H. N. Nguyen, J. Paulsen, S. Kumakura, M. H. Zhang, Y. S. Meng, *Adv. Energy Mater.* **2022**, *12*, 2103033.
[26] J. T. Zhao, X. Zhang, Y. Liang, Z. J. Han, S. Q. Liu, W. Q. Chu, H. J. Yu, *ACS Energy Lett.* **2021**, *6*, 2552.
[27] M. Z. Liu, J. Vatamanu, X. L. Chen, L. D. Xing, K. Xu, W. S. Li, *ACS Energy Lett.* **2021**, *6*, 2096.
[28] S. Y. Kim, C. S. Park, S. Hosseini, J. Lampert, Y. J. Kim, L. F. Nazar, *Adv. Energy Mater.* **2021**, *11*, 2100552.
[29] C. H. Yan, Q. N. Shao, Z. H. Yao, M. X. Gao, C. Y. Zhang, G. R. Chen, Q. W. Sun, W. P. Sun, Y. F. Liu, M. X. Gao, H. G. Pan, *Small* **2022**, *18*, 2107910.
[30] J. Chen, G. Q. Zou, W. T. Deng, Z. D. Huang, X. Gao, C. Liu, S. Y. Yin, H. Q. Liu, X. L. Deng, Y. Tian, J. Y. Li, C. W. Wang, D. Wang, H. W. Wu, L. Yang, H. S. Hou, X. B. Ji, *Adv. Funct. Mater.* **2020**, *30*, 2004302.
[31] J. X. Meng, L. S. Xu, Q. X. Ma, M. Q. Yang, Y. Z. Fang, G. Y. Wan, R. H. Li, J. J. Yuan, X. K. Zhang, H. J. Yu, L. L. Liu, T. F. Liu, *Adv. Funct. Mater.* **2022**, *32*, 2113013.
[32] J. M. Sun, C. C. Sheng, X. Cao, P. F. Wang, P. He, H. J. Yang, Z. Chang, X. Y. Yue, H. S. Zhou, *Adv. Funct. Mater.* **2022**, *32*, 2110295.
[33] Z. Zhu, D. W. Yu, Y. Yang, C. Su, Y. M. Huang, Y. H. Dong, I. Waluyo, B. M. Wang, A. Hunt, X. H. Yao, J. Lee, W. J. Xue, J. Li, *Nat. Energy* **2019**, *4*, 1049.
[34] S. M. Zhang, H. T. Gu, H. G. Pan, S. H. Yang, W. B. Du, X. Li, M. X. Gao, Y. F. Liu, M. Zhu, L. Z. Ouyang, D. C. Jian, F. Pan, *Adv. Energy Mater.* **2017**, *7*, 1601066.
[35] G. H. Zhang, B. Qiu, Y. G. Xia, X. L. Wang, Q. W. Gu, Y. B. Jiang, Z. L. He, Z. P. Liu, *J. Power Sources* **2019**, *420*, 29.
[36] J. T. Zhao, Y. Liang, X. Zhang, Z. H. Zhang, E. R. Wang, S. M. He, B. Y. Wang, Z. J. Han, J. Lu, K. Amine, H. J. Yu, *Adv. Funct. Mater.* **2021**, *31*, 2009192.
[37] Q. N. Shao, P. Y. Gao, C. H. Yan, M. X. Gao, W. B. Du, J. Chen, Y. X. Yang, J. T. Gan, Z. J. Wu, C. Y. Zhang, G. R. Chen, X. S. Zheng, Y. Lin, Y. Z. Jiang, W. P. Sun, Y. F. Liu, M. X. Gao, H. G. Pan, *Adv. Mater.* **2022**, *34*, 2108543.
[38] Y. H. Bian, L. Su, Z. C. Yu, Z. C. Lv, H. Chen, Y. Zhou, C. Meng, H. P. Du, M. Cai, H. N. Cao, M. C. Lin, *Electrochim. Acta* **2020**, *332*, 135188.
[39] L. F. Yang, K. L. Zhuo, X. C. Xu, Z. Z. Zhang, Q. Z. Du, Y. J. Chen, D. Sun, J. J. Wang, *J. Mater. Chem. A* **2020**, *8*, 21789.
[40] D. Sun, Y. Shen, W. Zhang, L. Yu, Z. Q. Yi, W. Yin, D. Wang, Y. H. Huang, J. Wang, D. L. Wang, J. B. Goodenough, *J. Am. Chem. Soc.* **2014**, *136*, 8941.
[41] Y. Ma, J. T. Li, X. B. Liao, W. Luo, W. Z. Huang, J. S. Meng, Q. Chen, S. B. Xi, R. H. Yu, Y. Zhao, L. Zhou, L. Q. Mai, *Adv. Funct. Mater.* **2020**, *30*, 2005000.
[42] J. S. Cao, M. Guan, G. H. Cao, Y. P. Zeng, J. M. Li, D. S. Qin, *Chin. Phys. Lett.* **2008**, *25*, 719.
[43] H. C. Zhang, R. Zhang, X. J. Liu, F. Ding, C. S. Shi, Z. Zhou, N. Q. Zhao, *J. Mater. Chem. A* **2021**, *9*, 24915.
[44] B. Zhang, L. Wang, X. Wang, S. Zhou, A. Fu, Y. Yan, Q. Wang, Q. Xie, D. Peng, Y. Qiao, *Energy Storage Mater.* **2022**, *53*, 492.
[45] B. Zhang, X. Wu, H. Luo, H. Yan, Y. Chen, S. Zhou, J. Yin, K. Zhang, H.-G. Liao, Q. Wang, *J. Am. Chem. Soc.* **2024**, *146*, 4557.
[46] B. Zhang, H. Zhang, H. Luo, H. Hua, X. Wu, Y. Chen, S. Zhou, J. Yin, K. Zhang, H. G. Liao, *Angew. Chem., Int. Ed.* **2024**, *63*, e202316790.
[47] S. Dong, Y. Zhou, C. Hai, J. Zeng, Y. Sun, Y. Shen, X. Li, X. Ren, C. Sun, G. Zhang, *J. Power Sources* **2020**, *462*, 228185.
[48] H. Zheng, C. Zhang, Y. Zhang, L. Lin, P. Liu, L. Wang, Q. Wei, J. Lin, B. Sa, Q. Xie, *Adv. Funct. Mater.* **2021**, *31*, 2100783.
[49] B. Zhang, Y. Zhang, X. Wang, H. Liu, Y. Yan, S. Zhou, Y. Tang, G. Zeng, X. Wu, H.-G. Liao, *J. Am. Chem. Soc.* **2023**, *145*, 8700.
[50] X. He, L. Meng, Y. Liu, X. Zhang, Z. Cheng, H. Huang, R. He, H. Pan, Y. Kang, J. Li, *Small* **2022**, *18*, 2202969.
[51] X. Chi, Q. Chen, Z. A. Lan, X. Zhang, X. Chen, X. Wang, *Chem. Euro. J.* **2023**, *29*, e202202734.
[52] X. W. Liu, A. R. Zhang, R. Ma, B. Wu, T. Wen, Y. J. Ai, M. T. Sun, J. Jin, S. H. Wang, X. K. Wang, *Chin. Chem. Lett.* **2022**, *33*, 3549.
[53] C. Zhao, Z. F. Chen, W. Wang, P. X. Xiong, B. F. Li, M. J. Li, J. X. Yang, Y. H. Xu, *Angew. Chem.-Int. Ed.* **2020**, *59*, 11992.
[54] R. Z. Yu, M. N. Banis, C. H. Wang, B. Wu, Y. Huang, S. Cao, J. J. Li, S. Jamil, X. T. Lin, F. P. Zhao, W. H. Lin, B. B. Chang, X. K. Yang, H. Huang, X. Y. Wang, X. L. Sun, *Energy Storage Mater.* **2021**, *37*, 509.
[55] Q. Y. Li, D. Ning, D. Wong, K. An, Y. X. Tang, D. Zhou, G. Schuck, Z. H. Chen, N. A. Zhang, X. F. Liu, *Nat. Commun.* **2022**, *13*, 1123.
[56] X. D. Zhang, J. L. Shi, J. Y. Liang, Y. X. Yin, J. N. Zhang, X. Q. Yu, Y. G. Guo, *Adv. Mater.* **2018**, *30*, 1801751.

[57] W. Zhu, Z. G. Tai, C. Y. Shu, S. K. Chong, S. W. Guo, L. J. Ji, Y. Z. Chen, Y. N. Liu, *J. Mater. Chem. A* **2020**, *8*, 7991.
[58] B. Xiao, H. Liu, N. Chen, M. N. Banis, H. Yu, J. Liang, Q. Sun, T. K. Sham, R. Li, M. Cai, *Angew. Chem., Int. Ed.* **2020**, *59*, 14313.
[59] J. Sun, C. Sheng, X. Cao, P. Wang, P. He, H. Yang, Z. Chang, X. Yue, H. Zhou, *Adv. Funct. Mater.* **2022**, *32*, 2110295.
[60] P. Yan, J. Zheng, Z.-K. Tang, A. Devaraj, G. Chen, K. Amine, J.-G. Zhang, L.-M. Liu, C. Wang, *Nat. Nanotechnol.* **2019**, *14*, 602.
[61] Z. Zhu, D. Yu, Y. Yang, C. Su, Y. Huang, Y. Dong, I. Waluyo, B. Wang, A. Hunt, X. Yao, *Nat. Energy* **2019**, *4*, 1049.
[62] J. Liu, F. Li, L. Xi, Z. Sun, Y. Yang, J. Shen, S. Yao, J. Zhao, M. Zhu, J. Liu, *Small* **2024**, *20*, 2305606.
[63] C. Wu, S. Cao, H. Li, Z. Li, G. Chen, X. Guo, B. Chang, Y. Bai, X. Wang, *Chem. Eng. J.* **2022**, *431*, 134208.
[64] W. Du, Y. Zheng, X. Liu, J. Cheng, R. C. K. Reddy, A. Zeb, X. Lin, Y. Luo, *Chem. Eng. J.* **2023**, *451*, 138626.
[65] X. Li, Z. H. Ren, M. N. Banis, S. X. Deng, Y. Zhao, Q. Sun, C. H. Wang, X. F. Yang, W. H. Li, J. W. Liang, X. N. Li, Y. P. Sun, K. Adair, R. Y. Li, Y. F. Hu, T. K. Sham, H. Huang, L. Zhang, S. G. Lu, J. Luo, X. L. Sun, *ACS Energy Lett.* **2019**, *4*, 2480.
[66] H. K. Schmid, W. Mader, *Micron.* **2006**, *37*, 426.
[67] W. B. Guo, Y. G. Zhang, L. Lin, W. He, H. F. Zheng, J. Lin, B. S. Sa, Q. L. Wei, L. S. Wang, Q. S. Xie, D. L. Peng, *Nano Energy* **2022**, *97*, 107201.
[68] M. Sathiya, G. Rousse, K. Ramesha, C. P. Laisa, H. Vezin, M. T. Sougrati, M. L. Doublet, D. Foix, D. Gonbeau, W. Walker, A. S. Prakash, M. Ben Hassine, L. Dupont, J. M. Tarascon, *Nat. Mater.* **2013**, *12*, 827.
[69] P. X. Bai, X. Ji, J. X. Zhang, W. R. Zhang, S. Hou, H. Su, M. J. Li, T. Deng, L. S. Cao, S. F. Liu, X. Z. He, Y. H. Xu, C. S. Wang, *Angew. Chem.-Int. Ed.* **2022**, *61*, 202202731.
[70] M. Yoon, Y. Dong, Y. Yoo, S. Myeong, J. Hwang, J. Kim, S. H. Choi, J. Sung, S. J. Kang, J. Li, J. Cho, *Adv. Funct. Mater.* **2020**, *30*, 1907903.
[71] J. G. Han, K. Kim, Y. Lee, N. S. Choi, *Adv. Mater.* **2019**, *31*, 1804822.
[72] C. Zhan, T. P. Wu, J. Lu, K. Amine, *Energy Environ. Sci.* **2018**, *11*, 243.
[73] W. Liu, J. X. Li, W. T. Li, H. Y. Xu, C. Zhang, X. P. Qiu, *Nat. Commun.* **2020**, *11*, 3629.
[74] S. Zhang, H. Gu, H. Pan, S. Yang, W. Du, X. Li, M. Gao, Y. Liu, M. Zhu, L. Ouyang, *Adv. Energy Mater.* **2017**, *7*, 1601066.
[75] C. Yan, Q. Shao, Y. Yang, M. Gao, Y. Lin, M. Gao, Z. Chen, Y. Wei, Y. Liu, W. Sun, *Adv. Funct. Mater.* **2024**, *34*, 2310873.